NeuroImage 200 (2019) 191–198

Contents lists available at ScienceDirect

NeuroImage

journal homepage: www.elsevier.com/locate/neuroimage

Quantitative magnetization transfer imaging of the human locus coeruleus

Paula Trujillo [a,*], Kalen J. Petersen [a], Matthew J. Cronin [b], Ya-Chen Lin [c], Hakmook Kang [c], Manus J. Donahue [a,b,d,e], Seth A. Smith [b,d,f], Daniel O. Claassen [a]

[a] Department of Neurology, Vanderbilt University Medical Center, Nashville, TN, USA
[b] Vanderbilt University Institute of Imaging Science, Vanderbilt University Medical Center, Nashville, TN, USA
[c] Department of Biostatistics, Vanderbilt University Medical Center, Nashville, TN, USA
[d] Department of Radiology and Radiological Sciences, Vanderbilt University Medical Center, Nashville, TN, USA
[e] Department of Psychiatry, Vanderbilt University Medical Center, Nashville, TN, USA
[f] Department of Biomedical Engineering, Vanderbilt University, Nashville, TN, USA

ARTICLE INFO

Keywords:
Locus coeruleus
MRI
Magnetization transfer
Neuromelanin

ABSTRACT

The locus coeruleus (LC) is the major origin of norepinephrine in the central nervous system, and is subject to age-related and neurodegenerative changes, especially in disorders such as Parkinson's disease and Alzheimer's disease. Previous studies have shown that neuromelanin (NM)-sensitive MRI can be used to visualize the LC, and it is hypothesized that magnetization transfer (MT) effects are the primary source of LC contrast. The aim of this study was to characterize the MT effects in LC imaging by applying high spatial resolution quantitative MT (qMT) imaging to create parametric maps of the macromolecular content of the LC and surrounding tissues. Healthy volunteers ($n = 26$; sex = 17 F/9M; age = 41.0 ± 19.1 years) underwent brain MRI on a 3.0 T scanner. qMT data were acquired using a 3D MT-prepared spoiled gradient echo sequence. A traditional NM scan consisting of a T_1-weighted turbo spin echo sequence with MT preparation was also acquired. The pool-size ratio (PSR) was estimated for each voxel using a single-point qMT approach. The LC was semi-automatically segmented on the MT-weighted images. The MT-weighted images provided higher contrast-ratio between the LC and surrounding pontine tegmentum (PT) (0.215 ± 0.031) than the reference images without MT-preparation (-0.005 ± 0.026) and the traditional NM images (0.138 ± 0.044). The PSR maps showed significant differences between the LC (0.090 ± 0.009) and PT (0.188 ± 0.025). The largest difference between the PSR values in the LC and PT was observed in the central slices, which also correspond to those with the highest contrast-ratio. These results highlight the role of MT in generating NM-related contrast in the LC, and should serve as a foundation for future studies aiming to quantify pathological changes in the LC and surrounding structures *in vivo*.

1. Introduction

The locus coeruleus (LC), a thin and elongated nucleus (average dimensions: length = 14.5 mm, width = 2.5 mm) located in the dorsal aspect of the pons in proximity to the fourth ventricle, is the major origin of norepinephrine (NE) in the central nervous system (CNS). It innervates extensive areas of the CNS, including the spinal cord, brain stem, cerebellum, and cerebral cortex, and has major roles in arousal, memory, attention, pain modulation, and stress response (Aston-Jones and Cohen, 2005; Benarroch, 2009; Hämmerer et al., 2018; Robbins, 1984; Samuels and Szabadi, 2008a). Pathological alterations to the LC-NE system have been associated with several neurological disorders including Alzheimer's disease (AD), Parkinson's disease (PD), Multiple System Atrophy (MSA), and Dementia with Lewy Bodies (DLB) (Samuels and Szabadi, 2008b). In early-stage AD, the LC degenerates, with marked neuronal loss and vulnerability to the occurrence of neurofibrillary tangles (Betts et al., 2019a; Braak et al., 2011). In PD, loss of LC neurons precedes degeneration of dopaminergic neurons of the substantia nigra (SN) pars compacta, and is associated with non-motor symptoms such as depression and sleep disturbances (Braak et al., 2003). Understanding early pathological changes of the LC and their role in disease progression may provide a basis for symptomatic pharmacotherapies. As such, there is a need

Abbreviations: CC, cerebral crus; LC, locus coeruleus; MT, magnetization transfer; NM, Neuromelanin; PD, Parkinson's Disease; PSR, pool size ratio; PT, pontine tegmentum; qMT, quantitative MT; RF, radiofrequency; SN, Substantia Nigra; TSE, turbo spin echo.

* Corresponding author. Department of Neurology Vanderbilt University Medical Center 1500 21st Ave South, Suite 1532, Nashville, TN, 37212, USA.
E-mail address: paula.trujillo.diaz@vumc.org (P. Trujillo).

https://doi.org/10.1016/j.neuroimage.2019.06.049
Received 15 February 2019; Received in revised form 17 June 2019; Accepted 19 June 2019
Available online 21 June 2019

for *in vivo* non-invasive LC biomarkers to offer insights into prognosis and treatment options.

Magnetic resonance imaging (MRI) allows for *in vivo* visualization of the LC by exploiting the presence of neuromelanin (NM), a pigment comprised of a polymer of 5,6-dihydroxyindole monomers that results from the oxidation of NE in the LC and dopamine in the SN. NM normally accumulates with age in the LC and SN (Liu et al., 2019; Zecca et al., 2001; Zucca et al., 2006), but is diminished in patients with pathological conditions involving LC degeneration (Zecca et al., 2006; Zucca et al., 2006). NM-sensitive MRI (NM-MRI) allows the investigation of the LC *in vivo* (Sasaki et al., 2006; Sulzer et al., 2018), with studies indicating that NM-MRI can detect alterations to LC (for a review, see (Betts et al., 2019b; Liu et al., 2017)), even in early disease stages (Miyoshi et al., 2013; Schwarz et al., 2011). Recent work has shown that the coeruleus/subcoeruleus complex is affected even in patients with idiopathic rapid eye movement (REM) sleep behavior disorder (RBD) (Ehrminger et al., 2016), which can precede overt symptoms of alpha-synucleinopathies by many years (Claassen et al., 2010; Iranzo et al., 2006; Schenck et al., 2013). These findings suggest that NM-MRI provides an early indicator of LC pathology, with potential application as a biomarker in prodromal stages of neurodegeneration. Additionally, a direct comparison between post-mortem NM-MRI and neuropathology (Keren et al., 2015) found that the LC contrast in NM-MRI corresponds to the location of NM-containing, NE-producing LC neurons, indicating that NM is the primary biological contributor to the LC contrast and may have the potential to characterize neurodegeneration.

However, the underlying physical mechanisms by which the presence of NM gives rise to signal hyperintensities on MRI (Trujillo et al., 2017a), and the nature of the relationship between loss of NM-based signal hyperintensity and disease progression is still poorly characterized. NM-MRI was originally based on a two-dimensional T_1-weighted turbo spin-echo (TSE) pulse sequence (Sasaki et al., 2006). Given that 2D multi-slice TSE sequences are sensitive to magnetization transfer (MT) effects caused by the train of refocusing pulses (Dixon et al., 1990) and that explicit MT preparation of NM-MRI pulse sequences increases the contrast between the NM-containing structures and surrounding brain tissues, it is likely that MT is the primary source of NM-MRI contrast (Nakane et al., 2008; Schwarz et al., 2013). Explicit MT preparation has also been pre-pended to 3D gradient echo pulse sequences to produce contrast between NM–containing structures and their surroundings (Chen et al., 2014; Langley et al., 2015; Ogisu et al., 2013; Schwarz et al., 2011; Trujillo et al., 2015), with advantages in terms of resolution and scan time over TSE scans. Furthermore, recent studies of the LC using MT-weighted images at 7T showed that the contrast-ratio between LC and a reference region in the pontine tegmentum is enhanced by applying MT preparation, and suggested that MT-weighted sequences are the most appropriate method for visualizing the LC at 7T (Priovoulos et al., 2018; Tona et al., 2019).

Despite growing evidence that the contrast in NM-MRI is associated with MT effects, with several studies using different MRI modalities (e.g. TSE, gradient echo), different vendors (e.g. Philips, Siemens), and different fields (i.e. 1.5 T, 3T and 7T) showing that sequences with an explicit MT-preparation pulse show higher sensitivity in detecting NM-containing structures in the brain, a detailed quantification of such effects is still lacking. MT contrast in MRI is the result of the interaction between protons contained in tissue macromolecules and the surrounding mobile water protons. MT contrast can be generated by applying MT preparation to selectively saturate the macromolecular protons, which constantly transfer saturation with free water protons, resulting in an observed signal attenuation driven by the macromolecular composition of tissues. This effect can be evaluated using quantitative MT (qMT) techniques (Ramani et al., 2002; Sled and Pike, 2001; Yarnykh and Yuan, 2004) which provide quantitative indices of tissue composition including the macromolecular-to-free pool size ratio (PSR). Recent studies have shown that high spatial resolution PSR maps can be obtained in clinically relevant scan times (Smith et al., 2014; Trujillo et al., 2017b; Yarnykh et al., 2015), making qMT a viable approach to investigate the LC.

The aim of this study was to quantitatively characterize MT effects in the LC, using qMT to provide parametric mapping of the macromolecular content of the LC and surrounding tissues.

2. Methods

2.1. Image acquisition

Healthy volunteers (n = 26; sex = 17 F/9M; age = 41.0 ± 19.1 years (range = 20–72 years)) participated in the study. All subjects gave written informed consent in accordance with the Declaration of Helsinki, and the study was approved by the institutional review board of Vanderbilt University Medical Center.

Participants underwent brain MRI on a 3T scanner (Achieva, Philips Medical Systems, Best, The Netherlands) with a 32-channel head receive coil and dual channel body coil for transmission. An anatomical 3D T_1-weighted scan (MPRAGE; spatial resolution = $1 \times 1 \times 1\ mm^3$; TR/TE = 8.9/4.6 m s, acquisition time = 5 min 27 s) was obtained for localization purposes.

The qMT data were acquired using a 3D MT-prepared spoiled gradient echo (SPGR) sequence (Smith et al., 2006; Trujillo et al., 2017b), with TR/TE/α = 42 m s/2.9 m s/16°, SENSE factor = 1.5, field of view = $120 \times 120 \times 20\ mm^3$, acquired spatial resolution = $0.6 \times 0.6 \times 2$, reconstructed spatial resolution = $0.23 \times 0.23 \times 1\ mm^3$ (through the use of zero padding, matrix size = 512×512), and signal averages = 4. MT weighting was achieved using a 20 m s, single-lobed sinc-gauss pulse with $\Delta\omega = 2$ kHz and αMT = 850°. A reference image (without MT weighting) was acquired using the same parameters but $\Delta\omega = 100$ kHz, as the MT-related saturation is considered negligible at this frequency. The total acquisition time for qMT data was 11 min.

To correct for B_0 and B_1 inhomogeneities, B_0 and B_1 maps were acquired using fast 3D sequences with the same field of view as the above qMT sequence. B_0 maps were obtained using the dual-TE phase-difference method (Skinner and Glover, 1997) with $TR/TE_1/TE_2$ = 50/5.8/8.1 m s, α = 25°, acquired/reconstructed resolution = $1.8 \times 1.8 \times 2/0.5 \times 0.5 \times 1\ mm^3$. B_1 maps were obtained using the actual flip-angle imaging method (Yarnykh, 2007) with $TR_1/TR_2/TE$ = 30/130/5.7 m s, α = 60°, acquired/reconstructed resolution = $1.8 \times 1.8 \times 2/0.5 \times 0.5 \times 1\ mm^3$. Acquisition times were 1 min 39s for the B_0 map, and 2 min 39s for the B_1 map. T_1 mapping was performed using a multiple flip angle (MFA) acquisition with TR/TE = 20/5.3 m s, α = 5, 10, 15, 20, 25, 30°, acquired/reconstructed resolution = $1.2 \times 1.2 \times 2/0.5 \times 0.5 \times 1\ mm^3$, acquisition time = 1 min 56 s.

Finally, we acquired a traditional NM-MRI scan consisting of a T_1-weighted 2D multi-slice TSE sequence with MT preparation using a 20-ms single-lobed sinc-gauss pulse with $\Delta\omega = 2$ kHz and αMT of 600° (field of view = $216 \times 180 \times 20\ mm^3$, TR/TE = 670/12 m s, acquired/reconstructed resolution = $0.6 \times 0.6 \times 2/0.38 \times 0.38 \times 2\ mm^2$, 8 signal averages, acquisition time = 7 min).

For all sequences except the MPRAGE, the field-of-view was placed orthogonal to the floor of the fourth ventricle and covered the area between the superior colliculi and the superior cerebellar peduncles (Fig. 1A).

2.2. Image processing

All data analyses were performed in Matlab R2016a (Mathworks, Natick, MA). For each subject, all images were co-registered to the MT-weighted image using FLIRT (FSL v5.0.2.1, FMRIB, Oxford, UK) (Jenkinson and Smith, 2001) with six degrees of freedom, mutual information cost function, and spline interpolation. Following co-registration, non-brain tissues were removed from all images by applying a brain mask created using a threshold approach. The signal intensities of the MT-weighted images were normalized to the intensity of the reference

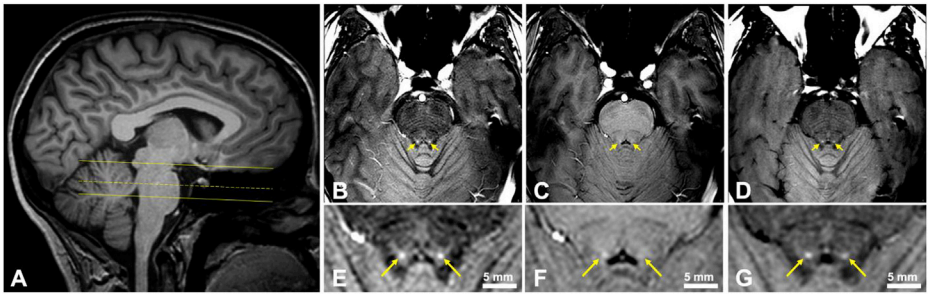

Fig. 1. Visualization of the LC. (A) Sagittal slice of the anatomical T1-weighted image illustrating the coverage of the field-of-view orthogonal to the floor of the fourth ventricle and covering the area between the superior colliculi and the superior cerebellar peduncles (solid lines), and the level of the axial view shown in B-D (dashed line). (B) Axial MT-weighted, (C) reference (no MT), and (D) 2D multi-slice TSE images. The area of the LC is magnified in (E) MT-weighted, (F) reference, and (G) 2D multi-slice TSE images (scale bars = 5 mm). The arrows indicate the location of the LC.

image ($\Delta\omega = 100$ kHz), and the nominal offset frequency and RF amplitudes were corrected using B_0 and B_1 maps, respectively. T_1 maps were reconstructed by fitting the Ernst equation with B_1 correction (Fram et al., 1987).

Subsequently, the pool-size ratio ($PSR = M_0^m/M_0^f$, where M_0^m and M_0^f are the equilibrium magnetization of the macromolecular and free pools, respectively) was estimated for each voxel using a single-point approach (Smith et al., 2017, 2014; Trujillo et al., 2017b; Yarnykh, 2012). The values used for the constrained parameters k_{mf}, $R_1^f T_2^f$, and T_2^m were 12.5 Hz, 0.018, and 10 μs, respectively, and were chosen based previous reports (Dortch et al., 2018; Trujillo et al., 2017b, 2015; Yarnykh, 2012). Cerebrospinal fluid (CSF) was excluded from the fitting by masking out the voxels with T_1 values greater than 3 s.

2.3. Tissue segmentation

The region of interest (ROI) for the LC was segmented manually on each MT-weighted image. The LC was defined on the axial plane in 10 slices. The inferior border was defined at the level of the superior cerebellar peduncles, and the superior border was defined at the level of the inferior colliculi. Similarly to (García-Lorenzo et al., 2013; Isaias et al., 2016; Priovoulos et al., 2018), on each of the 10 slices, we initially placed bilateral 9×9 voxel ($\sim 2.1 \times 2.1$ mm^2) ROIs around the hyperintense voxels at the lateral edge of the fourth ventricle (Fig. 2C and D). Then, we considered the voxels with the highest signal intensity within those ROIs to correspond to the LC area. Following the approach in (García-Lorenzo et al., 2013), for each slice and each side, we identified the 15 contiguous voxels with the highest signal intensity within the initial ROIs, and considered them the final LC ROI (Fig. 2E and F). The initial LC masks were placed manually by two independent raters (PT and KJP) using FSLeyes (FSL v5.0.2.1, FMRIB, Oxford, UK). All final LC ROIs were visually inspected. Reference 25×25 voxel ($\sim 5.9 \times 5.9$ mm^2) ROIs were defined bilaterally on each of the 10 slices in the rostral pontomesencephalic area (PT) (Betts et al., 2017; García-Lorenzo et al., 2013) (Fig. 2C).

As the SN also contains NM and shows similar hyperintensities on NM-MRI as the LC, we used additional ROIs in the SN for comparison. Bilateral 12×12 voxel ($\sim 2.8 \times 2.8$ mm^2) ROIs were placed in the medial portion of the SN and on the adjacent cerebral crus (CC) (Fig. 3) on 4 slices, starting at the level of superior limit of the inferior colliculi, which generally corresponds to 2 slices above the upper limit of the LC.

2.4. Signal quantification

As in most previous LC studies (for a review, see (Liu et al., 2017)), we first quantified the contrast ratio (CR) between the LC and the PT in the MT-weighted image, reference image (no-MT), and TSE NM-MRI. The CR between the LC and the PT was calculated for each slice and side of the LC as $CR_{LC}=(S_{LC}-S_{PT})/S_{PT}$, where S_{LC} and S_{PT} correspond to the mean signal intensity of the LC and PT, respectively, and was then averaged across sides and slices. For comparison, we also estimated the SN CR as $CR_{SN}=(S_{SN}-S_{CC})/S_{CC}$, where S_{SN} and S_{CC} correspond to the mean signal intensity of the SN and CC, respectively. The LC and PT ROIs were then used to sample the quantitative PSR and T_1 maps, and mean values and standard deviations were obtained for each ROI. PSR and T_1 means and standard deviations were also obtained in the SN and CC.

2.5. Statistical analysis

To assess the repeatability of the semi-automatic LC segmentation, the Dice coefficient was calculated to compare the LC segmentation obtained by the two raters. The difference between males and females was analyzed using Wilcoxon rank-sum test, and the differences between left

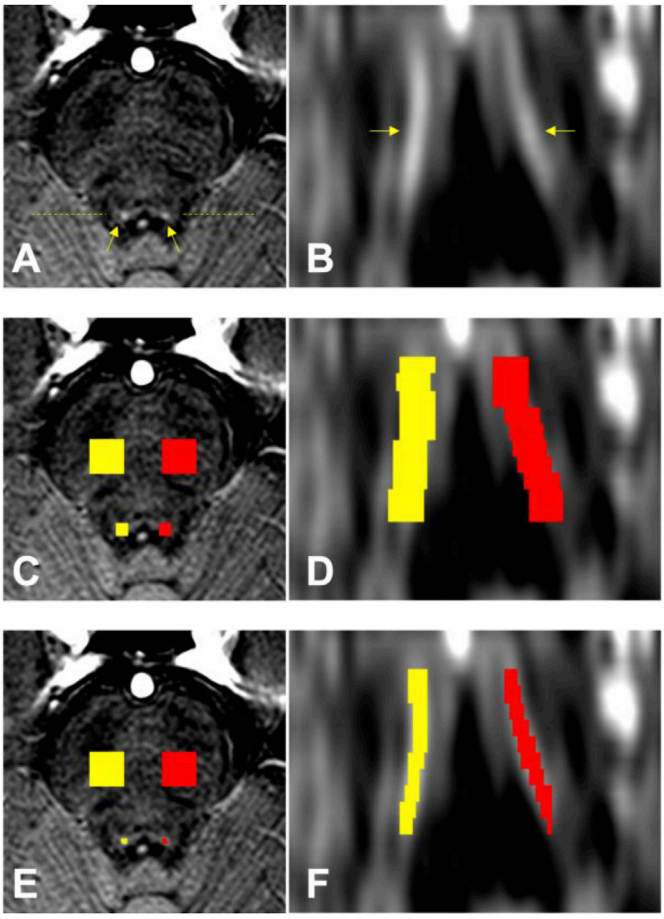

Fig. 2. Regions of interest for the LC and PT on the MT-weighted images. A) Axial view of the pons; the dashed line indicates the level of the coronal view shown in B, D and F, and the arrows indicate the location of the LC. B) Coronal view of the LC (arrows). C) Initial ROIs (9×9 voxel) around the LC and reference ROIs in the PT (25×25 voxel) on the left (red) and right (yellow) sides; D) Coronal view of the initial LC ROIs. E-F) Final LC ROI consisting of the 15 contiguous voxels (for each slice and side) with the highest signal intensity within the initial ROI.

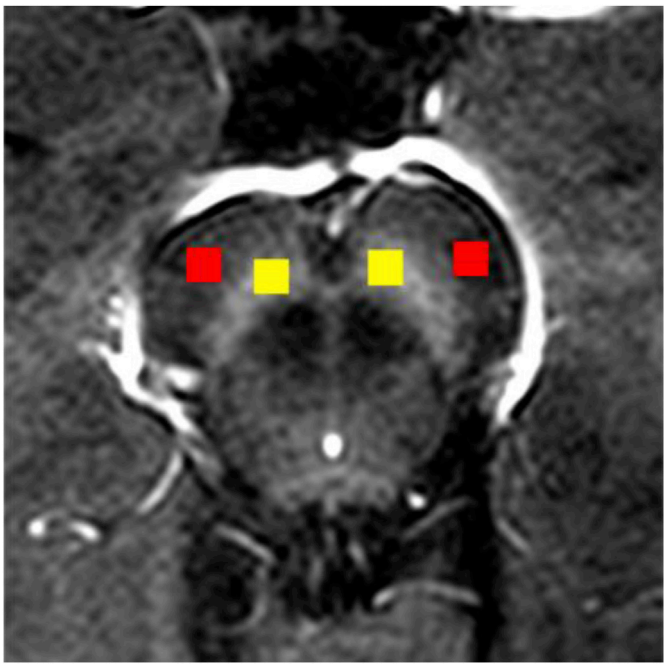

Fig. 3. Axial view of the midbrain at the level of the SN on an MT-weighted image showing the ROIs in the SN (yellow) and CC (red).

and right, different imaging modalities, and different ROIs were analyzed with a Wilcoxon signed-rank test. The correlations between age and CR_{LC}, age and PSR, and PSR and CR were evaluated using Spearman's rho correlation coefficient.

2.6. Data and code availability statement

The MRI data and Matlab code used in the present study are available at https://doi.org/10.17632/sx2yrz89w9.3 [dataset] (Trujillo, 2019).

3. Results

3.1. Locus coeruleus visualization and contrast ratio

In all participants, areas of hyperintensity were detected in the position of the LC in the MT-weighted and TSE NM-MRI images (Fig. 1). Conversely, the reference images provided poor LC contrast (Fig. 1F). The MT-weighted images provided significantly higher CR_{LC} compared to the TSE NM-MRI ($p < 0.001$) (Table 1). The highest CR_{LC} were observed in the central slices (Fig. 4A and B), while the lowest were observed in the rostral limits of the LC. There were significant differences in mean CR_{LC} between left and right sides. On average the right side had higher CR_{LC} (MT-weighted: 0.223 ± 0.034, $p = 0.007$; TSE NM-MRI: 0.139 ± 0.043, $p = 0.001$) compared to the left side (CR_{LC}: MT-weighted: 0.208 ± 0.032; TSE NM-MRI: 0.119 ± 0.038). On the contrary, there were no significant differences in CR_{SN} between left and right sides (CR_{SN} MT-weighted: Right $= 0.257 \pm 0.026$, Left $= 0.268 \pm 0.036$; $p = 0.069$; CR_{SN} TSE NM-MRI: Left $= 0.164 \pm 0.036$, Right $= 0.162 \pm 0.040$, $p = 0.778$). For all CRs, there were no significant differences between males and females. The CR_{LC} were not correlated with age (MT-weighted: rho $= 0.043$, $p = 0.834$; TSE NM-MRI: rho $= 0.082$, $p = 0.696$).

There was a high inter-rater agreement for the LC segmentation, with a mean Dice index of 0.96 (across slices and sides). The inter-rater Dice index varied across slices between 0.89 and 1, with lower values for the rostral LC, and higher agreement for the slices in the central portion (Table 1), which correspond to those with the highest CR_{LC} (Fig. 4A).

3.2. Quantitative magnetization transfer

An example of the PSR and T_1 maps for the LC is shown in Fig. 5. The PSR maps showed low values for the LC and higher values for the surrounding tissues in the superior cerebellar peduncles and pontomesencephalic area. The Wilcoxon test showed significant differences between the PSR values in the LC and PT ($p < 0.001$). Similarly, the CC showed significantly higher PSR values than the SN ($p < 0.001$) (Fig. 6). Table 2 summarizes the quantitative results for these ROIs. For all ROIs, there were no significant PSR differences between males and females.

The PSR values for the LC and PT varied across slices (Fig. 4B). The biggest difference between the PSR values in the LC and PT was observed in the central slices (Fig. 4C), which corresponded to those with the highest CR Finally, we observed that the difference in PSR between the PT and LC was significantly positively correlated with the CR_{LC} (rho $= 0.594$, $p < 0.001$) (Fig. 7).

4. Discussion

In this study, we applied qMT imaging to quantitatively characterize the MT effects in the LC. Previous studies had suggested that image contrast in the LC is predominated by MT effects, and here we provide a quantitative description of such effects. We found that high-resolution 3D gradient echo images with explicit MT preparation offered the highest CR_{LC} compared to the same images without MT preparation and the TSE NM-MRI images. Using the MT-prepared images, we applied qMT fitting to estimate the PSR, a measurement of the macromolecular content in tissue, and found lower PSR in the LC compared to surrounding areas of the PT. Furthermore, we found that the difference in PSR between the PT and LC was correlated with the CR_{LC}, suggesting that the LC contrast is related to the difference in macromolecular content between tissues.

Table 1
LC contrast ratio (CR_{LC}) and dice index. Mean ± standard deviation CR_{LC} across subjects for the 10 slices covering the LC from caudal (slice 1) to rostral (slice 10) for the three different imaging modalities.

	LC Contrast Ratio (CR_{LC})			Inter-rater Dice index		
Slice	MT-weighted	Reference	TSE NM-MRI	Left	Right	Mean
1	0.207 ± 0.08	−0.028 ± 0.050	0.060 ± 0.047	0.96	0.91	0.93
2	0.212 ± 0.06	−0.009 ± 0.030	0.106 ± 0.051	0.95	0.97	0.96
3	0.228 ± 0.051	−0.004 ± 0.034	0.149 ± 0.060	0.99	0.99	0.99
4	0.244 ± 0.048	0.006 ± 0.030	0.168 ± 0.045	0.98	1.00	0.99
5	0.248 ± 0.047	0.007 ± 0.033	0.168 ± 0.044	0.99	1.00	0.99
6	0.235 ± 0.043	0.004 ± 0.038	0.161 ± 0.056	0.98	1.00	0.99
7	0.216 ± 0.037	0.001 ± 0.036	0.147 ± 0.054	0.98	0.97	0.97
8	0.204 ± 0.032	−0.005 ± 0.036	0.138 ± 0.050	0.97	0.92	0.94
9	0.188 ± 0.029	−0.007 ± 0.028	0.125 ± 0.052	0.90	0.95	0.92
10	0.167 ± 0.031	−0.012 ± 0.030	0.120 ± 0.048	0.89	0.91	0.90
Mean	0.215 ± 0.031	−0.005 ± 0.026	0.138 ± 0.044	0.96	0.96	0.96

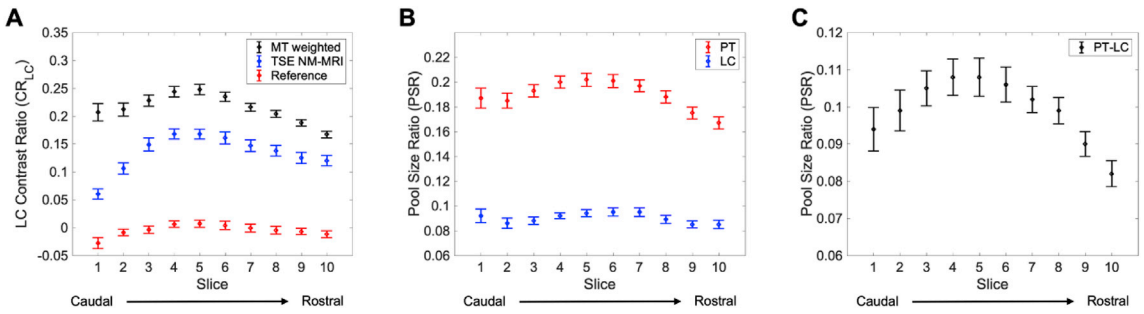

Fig. 4. A) Contrast-ratio (CR_{LC}) between the LC and the PT obtained from the MT-weighted (black), TSE NM-MRI (blue), and reference (red) images. B) PSR for the LC (blue) and PT (red). C) Difference in PSR between the PT and LC. The figures show the mean ± standard error of mean (SEM) across subjects for the 10 slices covering the LC.

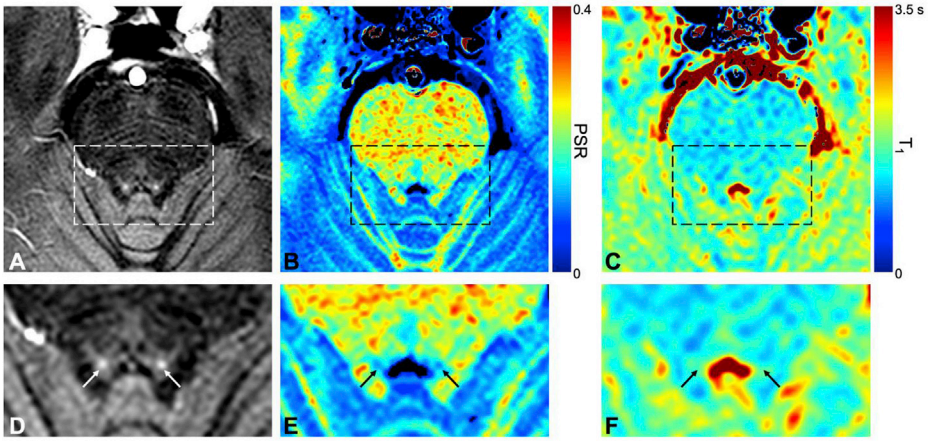

Fig. 5. (A) Axial MT-weighted image at the level of the LC. (B) PSR map. (C) T_1 map. The area around the LC indicated by the dashed rectangle is magnified in (D) MT-weighted, (E) PSR map, and (F) T_1 map. In D-F, the arrows indicate the location of the LC.

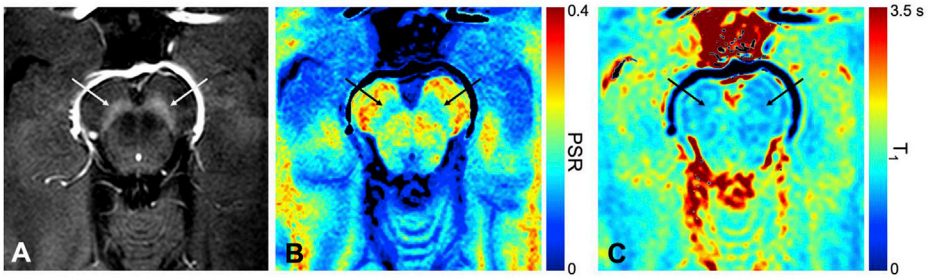

Fig. 6. A) Axial view of the midbrain at the level of the SN (arrows) on an MT-weighted image. B) PSR map. C) T_1 map.

Table 2
Quantitative PSR and T_1 values. Mean ± standard deviation for the different ROI.

ROI	PSR	T_1 (s)
Locus Coeruleus	0.090 ± 0.009	1.579 ± 0.262
Pontine Tegmentum	0.188 ± 0.025	1.226 ± 0.189
Substantia Nigra	0.115 ± 0.013	1.268 ± 0.181
Cerebral Crus	0.204 ± 0.027	1.136 ± 0.180

4.1. Contrast mechanisms

The main motivation for studying the qMT properties of the LC was to increase our understanding of the mechanisms underlying the NM-related contrast. Understanding the source of the contrast can inform about tissue composition and physiology, and provide basis to investigate pathological changes in different neurodegenerative diseases. Although there are currently multiple approaches to visualize the LC (for a review, see Liu et al., 2017), their underlying contrast mechanisms are still unclear. Post-mortem NM-MRI and neuropathological studies in the LC (Keren et al., 2015) have shown that the NM-MRI signal intensity is closely associated with the quantity of NM-containing neurons, raising the prospect that NM-MRI is a potential biomarker of LC neuronal integrity. NM is a complex pigment consisting of different components, including melanin, proteins, lipids, and metal ions such as iron and copper (Zecca et al., 2004, 2001). In NM, two iron-binding sites are present with different structures and iron affinities (Zucca et al., 2017) opening the possibility for unusual relaxation properties. In fact, the first study describing the NM-MRI technique (Sasaki et al., 2006) suggested that the source of the hyperintensity was paramagnetic T_1-shortening

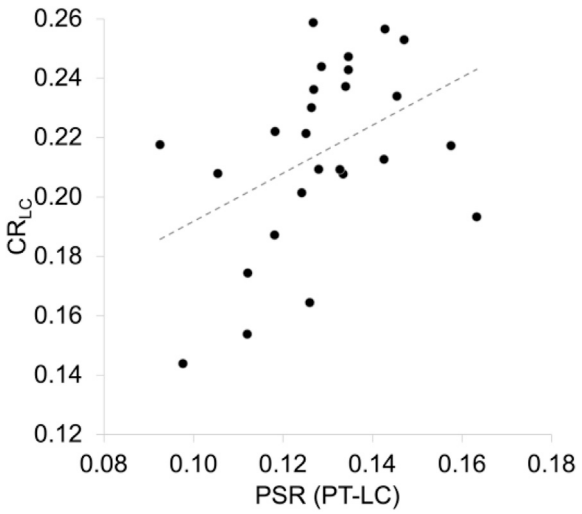

Fig. 7. Correlation between PSR (PT-LC) and CR_{LC}. The plot shows the mean values (across sides and slices) for each subject.

effects associated with the presence of NM. This idea has been supported by *in vitro* studies showing that the NM-iron complex produces concentration-dependent T_1 shortening effects (Enochs et al., 1997, 1989; Tosk et al., 1992; Trujillo et al., 2017a). However, these observations do not fully explain the contrast enhancement between NM-containing structures and surrounding tissues when MT preparation is performed, and in fact, it has been reported that T_1 values alone cannot account for the contrast seen in NM-MRI images (Hashido and Saito, 2016; Nakane et al., 2008). An *in vitro* study exploring the MT properties of NM (Trujillo et al., 2017a) showed that the NM-iron complex does not affect the PSR, and therefore does not directly alter the MT effect. However, as T_1 affects the MT saturation efficiency, the T_1 shortening induced by the presence of NM results in a reduction of the MT effect, similar to the effect of other paramagnetic ions (Tanttu et al., 1992). A such, the *in vivo* NM-MRI contrast may be the product of a combination of MT and T_1 effects, similar to MT-based background suppression in MR angiography (Thomas et al., 2002).

Here, we showed that the LC has lower PSR compared to surrounding tissues and that similarly, the SN has lower PSR than the CC (Trujillo et al., 2017b), reflecting the role of PSR in determining NM-related contrast. The PSR represents the proportion of the macromolecular protons (i.e. protons bound to immobile proteins, large macromolecules or cellular membranes) relative to the free water protons. The differences in PSR could be in part related to differences in myelin content, as myelin contributes to the restricted macromolecular pool, and consequently, differences in tissue myelination can lead to different PSR values. However, differences in water content, which are unrelated to myelin (e.g. edema, inflammation), can also cause changes in PSR. In fact, recent publications by Watanabe et al. (Watanabe et al., 2019b, 2019a) suggest that the high signal intensities in the LC are related to the high density of water protons. Our results are consistent with these publications, as low PSR indicates low macromolecular content and high free water content. Differences in PSR alone, however, do not completely explain the high signal intensity observed in the LC (and SN) in NM-MRI as other grey matter structures outside the brainstem show similar low PSR values (Figs. 4 and 5) but do not appear hyperintense in NM-MRI. We hypothesize that LC contrast is a mixture of properties of the LC and surrounding tissues, and that the LC hyperintensities are the results of the combination of low PSR (i.e. low macromolecular content/high free water content) and the shorter T_1 relative to other grey matter structures (due to the presence of NM). The combination of T_1-weighted imaging (present in both TSE and 3D-SPGR sequences) and MT-preparation results in saturation of white matter (due to higher PSR) and grey matter structures adjacent to the LC (due to higher PSR and/or longer T_1).

4.2. Advantages of quantitative LC imaging

The use of qMT provides several advantages compared to previous studies. Most LC imaging studies have used the signal intensity in a reference region (usually the PT) to normalize the LC signal (i.e. by calculating the CR) to allow for inter-subject and longitudinal assessments. This approach, however, presents several limitations as the signal in the reference tissue may change with age and can be affected by neurodegeneration (Keren et al., 2009, 2015). Here, we used qMT to obtain quantitative parametric maps, allowing inter-subject and longitudinal comparisons, which are not possible with weighted images. PSR is less dependent on the acquisition parameters, B_1 and B_0 inhomogeneities, T_1 and exchange times that affect traditional MT ratio (MTR) measures, and provides quantitative measurements in a voxel-wise manner, producing more detailed anatomical information than ROI approaches. This is relevant for studying the LC given its topographical distribution (Betts et al., 2017), as shown here by the different PSR values across its rostrocaudal extent.

4.3. Limitations

There are some caveats in the present study. Single-point PSR mapping provides a fast alternative to longer full-model qMT measurements (Smith et al., 2014; Trujillo et al., 2017b; Yarnykh et al., 2015), but has some practical limitations. We assumed fixed values for the remaining qMT parameters (i.e. k_{mf}, $R_1^f T_2^f$, and T_2^m) based on the values reported in previous studies showing that these values are relatively constant across tissues and across subjects. Previous qMT studies, however, were not focused on the LC, and it is possible that the selected values do not exactly correspond to the values in the LC area. Also, there is no evidence to support that these values remain constant across ageing. As the choice of these values, particularly k_{mf}, could affect the estimated PSR (Smith et al., 2014; Trujillo et al., 2017b), additional studies are necessary to obtain more accurate estimate of these parameters for the LC area. The PSR calculation also depends on T_1 values, and thus any error in T_1 mapping can propagate into the PSR. This could be particularly problematic in the rostral end of the LC, given its proximity to the fourth ventricle, which could cause partial volume effects from CSF.

4.4. Future directions

We observed higher LC contrast on the right side, similarly to the asymmetry reported by (Tona et al., 2017). However, other studies using 3T Siemens scanners have shown opposite asymmetry (Betts et al., 2017; Liu et al., 2019), suggesting that the asymmetry is not related to biological left/right differences, and that there is bias introduced by the direction of the magnetic field. These asymmetries could also be related to B_1 variations, and future LC imaging studies should investigate this issue further and incorporate field corrections. The sample size of this study is too small to investigate cross-sectional age effects, and studies with larger cohorts (e.g. Liu et al., 2019) are necessary to investigate such relationships. The increased signal to noise ratio (SNR) at ultra-high field MRI may offer the possibility of increasing the spatial resolution and reducing scan times and will play a role in future development of LC imaging (Priovoulos et al., 2018; Tona et al., 2019). The translation of pulsed off-resonance MT approaches to 7T, however, faces SAR limitations, and B_1 and B_0 inhomogeneities, and different approaches, such as inversion recovery (SIR) qMT imaging (Dortch et al., 2013; Tona et al., 2019) could provide an alternative for LC imaging at 7T.

One of the challenges for interpreting qMT imaging is that, like other MRI contrast mechanisms, MT is determined by processes on a molecular and atomic scale and, as a result, it is not specific to any single cellular mechanism. MT contrast within a voxel represents a combination of cell

types, cellular compartments, or even different tissues, and thus, interpretation of qMT results should benefit from supporting data from *in vitro* model systems and histopathology, as well as measurements using other imaging modalities. Future studies using multimodal quantitative MRI (e.g. high-resolution relaxometry and other multicompartment techniques such as biophysical models of diffusion) are necessary to disassociate the contributions from different cellular compartments (e.g. myelin, intra- and extra-cellular free water free water).

The effect of macromolecular changes to the LC in neuropathological conditions (e.g. alpha-synuclein aggregation and neuroinflammation in PD) remains to be tested, and future studies are required to determine if PSR can provide an index of LC degeneration. Finally, assessments for reproducibility, repeatability, sensitivity, specificity, and inter-vendor comparisons still need to be rigorously pursued before clinical adoption.

5. Conclusion

We characterized the MT effects in the LC by applying high-resolution qMT. We found that the macromolecular content, as measured by the PSR, was lower in the LC compared to surrounding areas in the PT, suggesting an MT contribution in determining NM-related contrast. These findings demonstrate the feasibility of performing qMT imaging of the LC providing a promising approach to investigate changes to the LC, and should serve as a foundation for future studies aiming to quantify pathological changes in the LC and surrounding structures *in vivo*, with potential application in the development of non-invasive biomarkers of neurodegeneration.

Financial disclosures

D.O.C. has received grant support from the National Institutes of Health, Michael J. Fox Foundation, as well as AbbVie, Bristol-Myers Squibb, C2N, CHDI, Eli Lilly, Teva, Vaccinex, and Wave Pharmaceuticals. D.O.C. has received personal fees from AbbVie, Acadia, Huntington Study Group, Lundbeck, Neurocrine, Teva Neuroscience, outside of submitted work. M.J.D. receives research related support from Philips North America and is the CEO of biosight, LLC which provides healthcare and technology consulting services.

Acknowledgments

We thank Kristen George-Durrett, Leslie McIntosh, Clair Jones, and Christopher Thompson for their assistance with the data acquisition. This work was supported by grants DOD W81XWH-13-0073, NIH/NIBIB R21 NS087465, NIH/NIBIB R01 EY023240, the National Multiple Sclerosis Society (RG-1501-02840), and the Conrad N. Hilton Foundation (17237) (to SAS), and by grant NIH/NINDS R01NS097783 (to DOC). This work was also supported by the NIH grant 1S10OD021771-01 for the 3T MRI, housed in the Vanderbilt Center for Human Imaging.

References

Aston-Jones, G., Cohen, J.D., 2005. An integrative theory of locus coeruleus-norepinephrine function: adaptive gain and optimal performance. Annu. Rev. Neurosci. 28, 403–450. https://doi.org/10.1146/annurev.neuro.28.061604.135709.

Benarroch, E.E., 2009. The locus ceruleus norepinephrine system: functional organization and potential clinical significance. Neurology 73, 1699–1704. https://doi.org/10.1212/WNL.0b013e3181c2937c.

Betts, M.J., Cardenas-Blanco, A., Kanowski, M., Jessen, F., Düzel, E., 2017. In vivo MRI assessment of the human locus coeruleus along its rostrocaudal extent in young and older adults. Neuroimage 163, 150–159. https://doi.org/10.1016/j.neuroimage.2017.09.042.

Betts, M.J., Cardenas-Blanco, A., Kanowski, M., Spottke, A., Teipel, S.J., Kilimann, I., Jessen, F., Düzel, E., 2019a. Locus coeruleus MRI contrast is reduced in Alzheimer's disease dementia and correlates with CSF Aβ levels. Alzheimer's Dement. Diagn. Assess. Dis. Monit. 11, 281–285. https://doi.org/10.1016/j.dadm.2019.02.001.

Betts, M.J., Kirilina, E., Otaduy, M., Ivanov, D., Acosta-Cabronero, J., Callaghan, M., Lambert, C., Cardenas-Blanco, A., Pine, K., Passamonti, L., Loane, C., Keuken, M.C., Trujillo, P., Lüsebrink, F., Mattern, H., Liu, K., Priovoulos, N., Fließbach, K., Dahl, M.J., Maaß, A., Madelung, C.F., Meder, D., Ehrenberg, A.J., Speck, O., Weiskopf, N., Dolan, R., Inglis, B., Tosun, D., Morawski, M., Zucca, F.A., Siebner, H.R., Mather, M., Uludag, K., Heinsen, H., Poser, B.A., Howard, R., Zecca, L., Rowe, J.B., Grinberg, L.T., Jacobs, H.I.L., Düzel, E., Hämmerer, D., 2019b. Locus coeruleus imaging as a biomarker for noradrenergic dysfunction in neurodegenerative diseases. Brain (in press). https://doi.org/10.1093/brain/awz193.

Braak, H., Del Tredici, K., Rüb, U., De Vos, R.A.I., Jansen Steur, E.N.H., Braak, E., 2003. Staging of brain pathology related to sporadic Parkinson's disease. Neurobiol. Aging 24, 197–211. https://doi.org/10.1016/S0197-4580(02)00065-9.

Braak, H., Thal, D.R., Ghebremedhin, E., Del Tredici, K., 2011. Stages of the pathologic process in alzheimer disease: age categories from 1 to 100 years. J. Neuropathol. Exp. Neurol. 70, 960–969. https://doi.org/10.1097/NEN.0b013e318232a379.

Chen, X., Huddleston, D.E., Langley, J., Ahn, S., Barnum, C.J., Factor, S.A., Levey, A.I., Hu, X., 2014. Simultaneous imaging of locus coeruleus and substantia nigra with a quantitative neuromelanin MRI approach. Magn. Reson. Imaging 32, 1301–1306. https://doi.org/10.1016/j.mri.2014.07.003.

Claassen, D.O., Josephs, K.A., Ahlskog, J.E., Silber, M.H., Tippmann-Peikert, M., Boeve, B.F., 2010. REM sleep behavior disorder preceding other aspects of synucleinopathies by up to half a century. Neurology 75, 494–499. https://doi.org/10.1212/WNL.0b013e3181ec7fac.

Dixon, W.T., Engels, H., Castillo, M., Sardashti, M., 1990. Incidental magnetization transfer contrast in standard multislice imaging. Magn. Reson. Imaging 8, 417–422.

Dortch, R.D., Bagnato, F., Gochberg, D.F., Gore, J.C., Smith, S.A., 2018. Optimization of selective inversion recovery magnetization transfer imaging for macromolecular content mapping in the human brain. Magn. Reson. Med. 80, 1824–1835. https://doi.org/10.1002/mrm.27174.

Dortch, R.D., Moore, J., Li, K., Jankiewicz, M., Gochberg, D.F., Hirtle, J.A., Gore, J.C., Smith, S.A., 2013. Quantitative magnetization transfer imaging of human brain at 7 T. Neuroimage 64, 640–649. https://doi.org/10.1016/j.neuroimage.2012.08.047.

Ehrminger, M., Latimier, A., Pyatigorskaya, N., Garcia-Lorenzo, D., Leu-Semenescu, S., Vidailhet, M., Lehericy, S.S., Arnulf, I., 2016. The coeruleus/subcoeruleus complex in idiopathic rapid eye movement sleep behaviour disorder. Brain 139, 1180–1188. https://doi.org/10.1093/brain/aww006.

Enochs, W., Petherick, P., Bogdanova, A., Mohr, U., Weissleder, R., 1997. Paramagnetic metal scavenging by melanin: MR imaging. Radiology 204, 417–423.

Enochs, W.S., Hyslop, W.B., Bennett, H.F., Brown, R.D., Koenig, S.H., Swartz, H.M., 1989. Sources of the increased longitudinal relaxation rates observed in melanotic melanoma. An in vitro study of synthetic melanins. Investig. Radiol. 24, 794–804.

Fram, E.K., Herfkens, R.J., Johnson, G.A., Glover, G.H., Karis, J.P., Shimakawa, A., Perkins, T.G., Pelc, N.J., 1987. Rapid calculation of T1 using variable flip angle gradient refocused imaging. Magn. Reson. Imaging 5, 201–208.

García-Lorenzo, D., Longo-Dos Santos, C., Ewenczyk, C., Leu-Semenescu, S., Gallea, C., Quattrocchi, G., Pita Lobo, P., Poupon, C., Benali, H., Arnulf, I., Vidailhet, M., Lehericy, S., 2013. The coeruleus/subcoeruleus complex in rapid eye movement sleep behaviour disorders in Parkinson's disease. Brain 136, 2120–2129. https://doi.org/10.1093/brain/awt152.

Hämmerer, D., Callaghan, M.F., Hopkins, A., Kosciessa, J., Betts, M., Cardenas-Blanco, A., Kanowski, M., Weiskopf, N., Dayan, P., Dolan, R.J., Düzel, E., 2018. Locus coeruleus integrity in old age is selectively related to memories linked with salient negative events. Proc. Natl. Acad. Sci. U. S. A. 115, 2228–2233. https://doi.org/10.1073/pnas.1712268115.

Hashido, T., Saito, S., 2016. Quantitative T1, T2, and T2* mapping and semi-quantitative neuromelanin-sensitive magnetic resonance imaging of the human midbrain. PLoS One 11, 1–15. https://doi.org/10.1371/journal.pone.0165160.

Iranzo, A., Molinuevo, J.L., Santamaría, J., Serradell, M., Martí, M.J., Valldeoriola, F., Tolosa, E., 2006. Rapid-eye-movement sleep behaviour disorder as an early marker for a neurodegenerative disorder: a descriptive study. Lancet Neurol. 5, 572–577. https://doi.org/10.1016/S1474-4422(06)70476-8.

Isaias, I.U., Trujillo, P., Summers, P., Marotta, G., Mainardi, L., Pezzoli, G., Zecca, L., Costa, A., 2016. Neuromelanin imaging and dopaminergic loss in Parkinson's disease. Front. Aging Neurosci. 8, 196. https://doi.org/10.3389/fnagi.2016.00196.

Jenkinson, M., Smith, S., 2001. A global optimisation method for robust affine registration of brain images. Med. Image Anal. 5, 143–156.

Keren, N., Lozar, C., Harris, K., Morgan, P., Eckert, M., 2009. In vivo mapping of the human locus coeruleus. Neuroimage 47, 1261–1267. https://doi.org/10.1016/j.neuroimage.2009.06.012.

Keren, N.I., Taheri, S., Vazey, E.M., Morgan, P.S., Granholm, A.-C.C.E., Aston-Jones, G.S., Eckert, M.A., 2015. Histologic validation of locus coeruleus MRI contrast in post-mortem tissue. Neuroimage 113, 235–245. https://doi.org/10.1016/j.neuroimage.2015.03.020.

Langley, J., Huddleston, D.E., Chen, X., Sedlacik, J., Zachariah, N., Hu, X., 2015. A multicontrast approach for comprehensive imaging of substantia nigra. Neuroimage 112, 7–13. https://doi.org/10.1016/j.neuroimage.2015.02.045.

Liu, K.Y., Acosta-Cabronero, J., Cardenas-Blanco, A., Loane, C., Berry, A.J., Betts, M.J., Kievit, R.A., Henson, R.N., Düzel, E., Howard, R., Hämmerer, D., 2019. In vivo visualization of age-related differences in the locus coeruleus. Neurobiol. Aging 74, 101–111. https://doi.org/10.1016/J.NEUROBIOLAGING.2018.10.014.

Liu, K.Y., Marijatta, F., Hämmerer, D., Acosta-Cabronero, J., Düzel, E., Howard, R.J., 2017. Magnetic resonance imaging of the human locus coeruleus: a systematic review. Neurosci. Biobehav. Rev. 83, 325–355. https://doi.org/10.1016/j.neubiorev.2017.10.023.

Miyoshi, F., Ogawa, T., Kitao, S.S., Kitayama, M., Shinohara, Y., Takasugi, M., Fujii, S., Kaminou, T., 2013. Evaluation of Parkinson disease and alzheimer disease with the use of neuromelanin MR imaging and 123I-metaiodobenzylguanidine scintigraphy. AJNR Am. J. Neuroradiol. 34, 2113–2118. https://doi.org/10.3174/ajnr.A3567.

Nakane, T., Nihashi, T., Kawai, H., Naganawa, S., 2008. Visualization of neuromelanin in the Substantia nigra and locus ceruleus at 1.5T using a 3D-gradient echo sequence with magnetization transfer contrast. Magn. Reson. Med. Sci. 7, 205–210.

Ogisu, K., Kudo, K., Sasaki, M., Sakushima, K., Yabe, I., Sasaki, H., Terae, S., Nakanishi, M., Shirato, H., 2013. 3D neuromelanin-sensitive magnetic resonance imaging with semi-automated volume measurement of the substantia nigra pars compacta for diagnosis of Parkinson's disease. Neuroradiology 55, 719–724. https://doi.org/10.1007/s00234-013-1171-8.

Priovoulos, N., Jacobs, H.I.L., Ivanov, D., Uludağ, K., Verhey, F.R.J., Poser, B.A., 2018. High-resolution in vivo imaging of human locus coeruleus by magnetization transfer MRI at 3T and 7T. Neuroimage 168, 427–436. https://doi.org/10.1016/j.neuroimage.2017.07.045.

Ramani, A., Dalton, C., Miller, D.H., Tofts, P.S., Barker, G.J., 2002. Precise estimate of fundamental in-vivo MT parameters in human brain in clinically feasible times. Magn. Reson. Imaging 20, 721–731. https://doi.org/10.1016/S0730-725X(02)00598-2.

Robbins, T.W., 1984. Cortical noradrenaline, attention and arousal. Psychol. Med. 14, 13–21. https://doi.org/10.1017/S0033291700003032.

Samuels, E.R., Szabadi, E., 2008a. Functional neuroanatomy of the noradrenergic locus coeruleus: its roles in the regulation of arousal and autonomic function part I: principles of functional organisation. Curr. Neuropharmacol. 6, 235–253. https://doi.org/10.2174/157015908785777229.

Samuels, E.R., Szabadi, E., 2008b. Functional neuroanatomy of the noradrenergic locus coeruleus: its roles in the regulation of arousal and autonomic function part II: physiological and pharmacological manipulations and pathological alterations of locus coeruleus activity in humans. Curr. Neuropharmacol. 6, 254–285. https://doi.org/10.2174/157015908785777193.

Sasaki, M., Shibata, E., Tohyama, K., Takahashi, J., Otsuka, K., Tsuchiya, K., Takahashi, S., Ehara, S., Terayama, Y., Sakai, A., 2006. Neuromelanin magnetic resonance imaging of locus ceruleus and substantia nigra in Parkinson's disease. Neuroreport 17, 1215–1218. https://doi.org/10.1097/01.wnr.0000227984.84927.a7.

Schenck, C.H., Boeve, B.F., Mahowald, M.W., 2013. Delayed emergence of a parkinsonian disorder or dementia in 81% of older men initially diagnosed with idiopathic rapid eye movement sleep behavior disorder: a 16-year update on a previously reported series. Sleep Med. 14, 744–748. https://doi.org/10.1016/j.sleep.2012.10.009.

Schwarz, S.T., Bajaj, N., Morgan, P.S., Reid, S., Gowland, P., Auer, D.P., 2013. Magnetisation Transfer contrast to enhance detection of neuromelanin loss at 3T in Parkinson's disease. Proc. Int. Soc. Mag. Reson. Med. 2848.

Schwarz, S.T., Rittman, T., Gontu, V., Morgan, P.P.S., Bajaj, N., Auer, D.D.P., 2011. T1-weighted MRI shows stage-dependent substantia nigra signal loss in Parkinson's disease. Mov. Disord. 26, 335–335. https://doi.org/10.1002/mds.23722.

Skinner, T., Glover, G., 1997. An extended two-point Dixon algorithm for calculating separate water, fat, and B0 images. Magn. Reson. Med. 37, 628–630.

Sled, J.G., Pike, G.B., 2001. Quantitative imaging of magnetization transfer exchange and relaxation properties in vivo using MRI. Magn. Reson. Med. 46, 923–931.

Smith, A.K., By, S., Lyttle, B.D., Dortch, R.D., Box, B.A., Mckeithan, L.J., Thukral, S., Bagnato, F., Pawate, S., Smith, S.A., 2017. Evaluating single-point quantitative magnetization transfer in the cervical spinal cord: application to multiple sclerosis. NeuroImage Clin. 16, 58–65. https://doi.org/10.1016/j.nicl.2017.07.010.

Smith, A.K., Dortch, R.D., Dethrage, L.M., Smith, S.A., 2014. Rapid, high-resolution quantitative magnetization transfer MRI of the human spinal cord. Neuroimage 95, 106–116. https://doi.org/10.1016/j.neuroimage.2014.03.005.

Smith, S.A., Farrell, J.A.D., Jones, C.K., Reich, D.S., Calabresi, P.A., van Zijl, P.C.M., 2006. Pulsed magnetization transfer imaging with body coil transmission at 3 Tesla: feasibility and application. Magn. Reson. Med. 56, 866–875. https://doi.org/10.1002/mrm.21035.

Sulzer, D., Cassidy, C., Horga, G., Kang, U.J., Fahn, S., Casella, L., Pezzoli, G., Langley, J., Hu, X.P., Zucca, F.A., Isaias, I.U., Zecca, L., 2018. Neuromelanin detection by magnetic resonance imaging (MRI) and its promise as a biomarker for Parkinson's disease. npj Parkinson's Dis. 4, 11. https://doi.org/10.1038/s41531-018-0047-3.

Tanttu, J.I., Sepponen, R.E., Lipton, M.J., Kuusela, T., 1992. Synergistic enhancement of MRI with Gd-DTPA and magnetization transfer. J. Comput. Assist. Tomogr. 16, 19–24.

Thomas, S.D., Al-Kwifi, O., Emery, D.J., Wilman, A.H., 2002. Application of magnetization transfer at 3.0 T in three-dimensional time-of-flight magnetic resonance angiography of the intracranial arteries. J. Magn. Reson. Imaging 15, 479–483.

Tona, K.-D., Keuken, M.C., de Rover, M., Lakke, E., Forstmann, B.U., Nieuwenhuis, S., van Osch, M.J.P., 2017. In vivo visualization of the locus coeruleus in humans: quantifying the test–retest reliability. Brain Struct. Funct. 222, 4203–4217. https://doi.org/10.1007/s00429-017-1464-5.

Tona, K.-D., van Osch, M.J.P., Nieuwenhuis, S., Keuken, M.C., 2019. Quantifying the contrast of the human locus coeruleus in vivo at 7 Tesla MRI. PLoS One 14, e0209842. https://doi.org/10.1371/journal.pone.0209842.

Tosk, J.M., Holshouser, B.A., Aloia, R.C., Hinshaw, D.B., Hasso, A.N., MacMurray, J.P., Will, A.D., Bozzetti, L.P., 1992. Effects of the interaction between ferric iron and L-dopa melanin on T1 and T2 relaxation times determined by magnetic resonance imaging. Magn. Reson. Med. 26, 40–45. https://doi.org/10.1002/mrm.1910260105.

Trujillo, P., Smith, A.K., Summers, P.E., Mainardi, L.M., Cerutti, S., Smith, S.A., Costa, A., 2015. High-resolution quantitative imaging of the substantia nigra. Conf. Proc. IEEE Eng. Med. Biol. Soc. 2015, 5428–5431. https://doi.org/10.1109/EMBC.2015.7319619.

Trujillo, P., Summers, P.E., Ferrari, E., Zucca, F.A., Sturini, M., Mainardi, L.T., Cerutti, S., Smith, A.K., Smith, S.A., Zecca, L., Costa, A., 2017a. Contrast mechanisms associated with neuromelanin-MRI. Magn. Reson. Med. 78, 1790–1800. https://doi.org/10.1002/mrm.26584.

Trujillo, P., Summers, P.E., Smith, A.K., Smith, S.A., Mainardi, L.T., Cerutti, S., Claassen, D.O., Costa, A., 2017b. Pool size ratio of the substantia nigra in Parkinson's disease derived from two different quantitative magnetization transfer approaches. Neuroradiology 59, 1251–1263. https://doi.org/10.1007/s00234-017-1911-2.

Trujillo, P., 2019. Quantitative magnetization transfer imaging of the human locus coeruleus. Mendeley Data V3. https://doi.org/10.17632/sx2yrz89w9.3.

Watanabe, T., Tan, Z., Wang, X., Martinez-Hernandez, A., Frahm, J., 2019a. Magnetic resonance imaging of noradrenergic neurons. Brain Struct. Funct. 0, 0. https://doi.org/10.1007/s00429-019-01858-0.

Watanabe, T., Wang, X., Tan, Z., Frahm, J., 2019b. Magnetic resonance imaging of brain cell water. Sci. Rep. 9, 5084. https://doi.org/10.1038/s41598-019-41587-2.

Yarnykh, V., 2007. Actual flip-angle imaging in the pulsed steady state: a method for rapid three-dimensional mapping of the transmitted radiofrequency field. Magn. Reson. Med. 57, 192–200.

Yarnykh, V.L., 2012. Fast macromolecular proton fraction mapping from a single off-resonance magnetization transfer measurement. Magn. Reson. Med. 68, 166–178. https://doi.org/10.1002/mrm.23224.

Yarnykh, V.L., Bowen, J.D., Samsonov, A., Repovic, P., Mayadev, A., Qian, P., Gangadharan, B., Keogh, B.P., Maravilla, K.R., Jung Henson, L.K., 2015. Fast whole-brain three-dimensional macromolecular proton fraction mapping in multiple sclerosis. Radiology 274, 210–220. https://doi.org/10.1148/radiol.14140528.

Yarnykh, V.L., Yuan, C., 2004. Cross-relaxation imaging reveals detailed anatomy of white matter fiber tracts in the human brain. Neuroimage 23, 409–424. https://doi.org/10.1016/j.neuroimage.2004.04.029.

Zecca, L., Gallorini, M., Schünemann, V., Trautwein, A.X., Gerlach, M., Riederer, P., Vezzoni, P., Tampellini, D., 2001. Iron, neuromelanin and ferritin content in the substantia nigra of normal subjects at different ages: consequences for iron storage and neurodegenerative processes. J. Neurochem. 76, 1766–1773.

Zecca, L., Stroppolo, A., Gatti, A., Tampellini, D., Toscani, M., Gallorini, M., Giaveri, G., Arosio, P., Santambrogio, P., Fariello, R.G., Karatekin, E., Kleinman, M.H., Turro, N., Hornykiewicz, O., Zucca, F.A., 2004. The role of iron and copper molecules in the neuronal vulnerability of locus coeruleus and substantia nigra during aging. Proc. Natl. Acad. Sci. U. S. A. 101, 9843–8. https://doi.org/10.1073/pnas.0403495101.

Zecca, L., Zucca, F., Albertini, A., Rizzio, E., Fariello, R.G., 2006. A proposed dual role of neuromelanin in the pathogenesis of Parkinson' s disease. Neurology 67, S8–S11.

Zucca, F., Bellei, C., Giannelli, S., Terreni, M., Gallorini, M., Rizzio, E., Pezzoli, G., Albertini, A., Zecca, L., 2006. Neuromelanin and iron in human locus coeruleus and substantia nigra during aging: consequences for neuronal vulnerability. J. Neural Transm. 113, 757–767. https://doi.org/10.1007/s00702-006-0453-2.

Zucca, F.A., Segura-Aguilar, J., Ferrari, E., Muñoz, P., Paris, I., Sulzer, D., Sarna, T., Casella, L., Zecca, L., 2017. Interactions of iron, dopamine and neuromelanin pathways in brain aging and Parkinson's disease. Prog. Neurobiol. 155, 96–119. https://doi.org/10.1016/j.pneurobio.2015.09.012.